2012

Compound Capillary Rise

Mark M. Weislogel
Portland State University, weisloge@pdx.edu

Citation Details
M.M. Compound Capillary Rise, J. Fluid Mech., Vol. 709, pp. 622-647, (2012).

J. Fluid Mech. (2012), *vol.* 709, *pp.* 622–647.
doi:10.1017/jfm.2012.357

Compound capillary rise

Mark M. Weislogel†

Department of Mechanical and Materials Engineering, Portland State University, PO Box 751, Portland, OR 97207, USA

(Received 19 January 2012; revised 28 April 2012; accepted 9 July 2012; first published online 23 August 2012)

Irregular conduits, complex surfaces, and porous media often manifest more than one geometric wetting condition for spontaneous capillary flows. As a result, different regions of the flow exhibit different rates of flow, all the while sharing common dynamical capillary pressure boundary conditions. The classic problem of sudden capillary rise in tubes with interior corners is revisited from this perspective and solved numerically in the self-similar $\sim t^{1/2}$ visco-capillary limit *à la* Lucas–Washburn. Useful closed-form analytical solutions are obtained in asymptotic limits appropriate for many practical flows in conduits containing one or more interior corner. The critically wetted corners imbibe fluid away from the bulk capillary rise, shortening the viscous column length and slightly increasing the overall flow rate. The extent of the corner flow is small for many closed conduits, but becomes significant for flows along open channels and the method is extended to approximate hemiwicking flows across triangular grooved surfaces. It is shown that an accurate application of the method depends on an accurate *a priori* assessment of the competing viscous cross-section length scales, and the expedient Laplacian scaling method is applied herein toward this effect.

Key words: capillary flows, channel flow, porous media

1. Introduction

The classic problem of capillary rise is sketched in figure 1(*a*) for flow in a right circular cylindrical tube. The wetting fluid with contact angle $\theta < \pi/2$ creates an under-pressure at the interface which draws the fluid up the tube as measured by column length $l(t)$. The impact of gravity is negligible if the tube diameter and rise height are small enough. The same flow is sketched in figure 1(*b*), but for capillary rise in a right square tube. In this situation, if the contact angle satisfies a second condition $\theta < \pi/2 - \alpha$, as described by Concus & Finn (1969) where α is the half-angle of the included corner angle, the liquid 'wets' the interior corners of the container and advances ahead of the bulk meniscus. In effect, there are thus two wetting conditions resulting in what is referred to as a compound capillary flow. In the absence of bulk flow, the corner flows act to drain the bulk region by imbibing the fluid into and along the interior corners of the container, as measured by the corner flow column length $\mathscr{L}(t)$ and sketched in figure 1(*c*). The compound flow of figure 1(*b*) is just a combination of bulk and corner flows.

A simple drop tower experiment for studying capillary rise in square tubes is depicted schematically in figure 2(*a*). In this test, following release of the experiment

† Email address for correspondence: mmw@cecs.pdx.edu

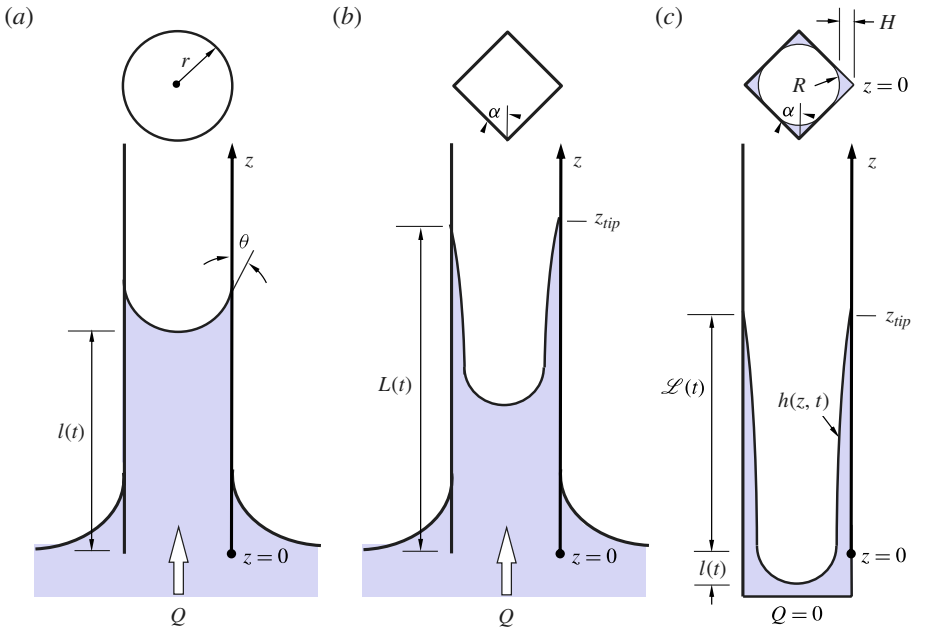

FIGURE 1. (Colour online) Sketches of (*a*) classical capillary rise in a right circular cylinder with wetting fluid of contact angle θ, (*b*) compound capillary rise in a right square tube with interior corner flow, and (*c*) pure interior corner flow (imbibition) with inlet flow $Q = 0$. Note that $l(t) < 0$ in (*c*), which might also be considered a compound capillary flow as the corner flows draw down the bulk meniscus.

into free fall, the sudden capillary rise induced in a 3.5 mm diameter square tube partially immersed in a reservoir of perfectly wetting 0.65 cS polydimethylsiloxane is imaged by video camera at 60 fps. Selected frames are presented in figure 2(*b*) for the 2.13 s reduced acceleration period of the 22 m drop ($\lesssim 10^{-4} g_o$, where $g_o = 9.8$ m s^{-2}). See Wollman (2012) for further drop tower details. The images show transitions from low-g interface formation and high-speed inertial and viscous corner flows (images 1–2), to one or more bulk meniscus inertial regimes (images 1–5), before establishment of the fully developed viscous compound capillary flow (images 5–13). The bulk flow and corner flow lengths $l(t)$ and $\mathscr{L}(t)$ are approximated on the figure, where both are found to lengthen with $t^{1/2}$ at long times. Quantifying the ratio of these lengths is an objective of this primarily analytical work. A detailed experimental verification will await a subsequent publication.

Both bulk and corner flows have been studied thoroughly, but separately. Bulk flow was addressed originally by Lucas (1918), Washburn (1921) and others, receiving perhaps its final treatments by Quéré (1997) and Stange, Dreyer & Rath (2003). The corner flow problem was first solved by Dong & Chatzis (1995) with later attention given by Romero & Yost (1996), Weislogel & Lichter (1998) and others. These solutions will be briefly reviewed as a means to introduce both the notation and the primary assumptions for the new compound solutions. The atypical Laplacian scaling method of Weislogel, Chen & Bolledulla (2008) is employed to generalize the presentation. The final result is a simple numerical similarity solution with well-established asymptotic limits. Closed-form analytic expressions are found in widely applicable limiting regimes. The general approach is useful for explaining observations

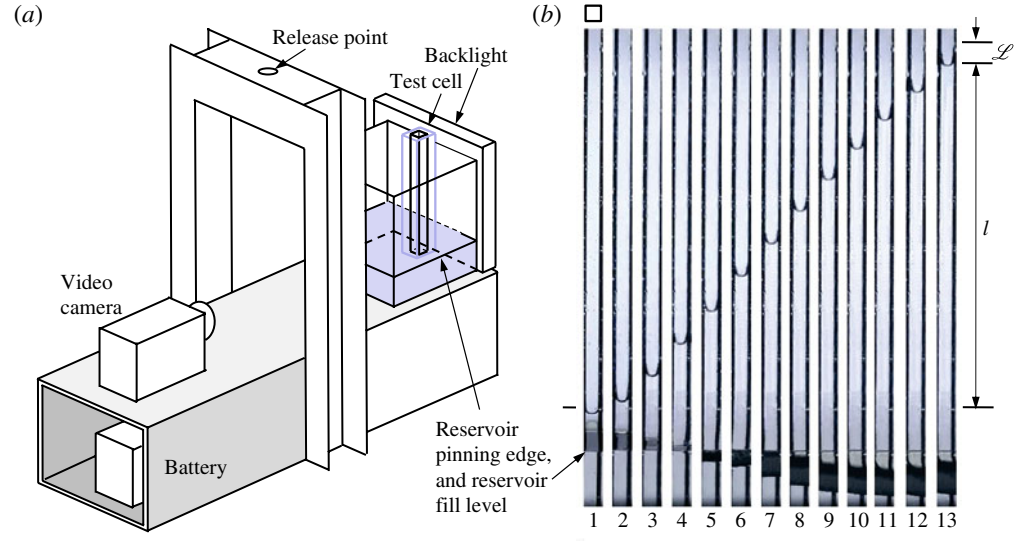

FIGURE 2. (Colour online) (*a*) Schematic of a simple drop tower experiment rig with 3.5 mm square tube test cell (not to scale). The experiment rig is released in an aerodynamically shielded chamber and falls 22 m (2.13 s). (*b*) Selected images at 0.167 s intervals during the compound capillary rise (frame 1 at $t = 0$ s, frame 13 at $t = 2$ s). Approximate advancing bulk and corner flow locations $l(t)$ and $\mathscr{L}(t)$ are identified on the right.

of more complex flows, as well as guiding the geometric design of wetting systems including wicking flows over complex surfaces.

2. Review and notation

In the visco-capillary limit, capillary flows along conduits are governed by Laplace's equation

$$P_z = \mu \Delta w, \tag{2.1}$$

where P_z is the capillary pressure gradient along the conduit z-direction, μ is the fluid dynamic viscosity, Δ is the Laplacian operator, and $w = w(x, y, t)$ is the z-component of velocity. Application of (2.1) assumes the quasi-steady fully developed laminar flow of a slender column of fluid and ignores complicating effects of three-dimensional flows in the vicinity of moving menisci, entrance regions, and the properties of the displaced fluid. Further complications are avoided by assuming flows slow enough such that changes in dynamic interface curvature may be neglected, as well as other issues associated with the moving contact line boundary condition, Kistler (1993). Often just for scaling purposes, but employed here for rather quantitative results, for convex conduit cross-sections, (2.1) may be 'solved' algebraically for the average velocity

$$\langle w \rangle = -F_i \frac{P_z}{\mu \Delta_s}, \tag{2.2}$$

where

$$\Delta_s \equiv \frac{1}{x_s^2} + \frac{1}{y_s^2} \sim \Delta \equiv \frac{\partial^2}{\partial x^2} + \frac{\partial^2}{\partial y^2}, \tag{2.3}$$

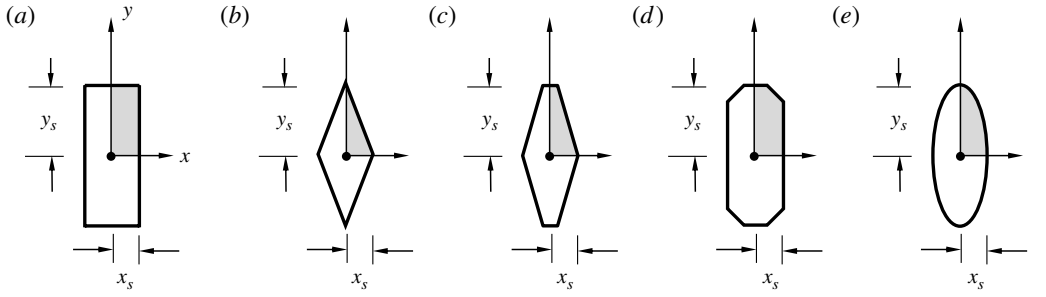

FIGURE 3. Selection of applicable convex conduit sections where the Laplacian scaling method is particularly useful: (*a*) rectangles, (*b*) rhombi, blunt (*c*) rhombi and (*d*) rectangles, and (*e*) ellipses. The shaded upper right region of each section identifies the 'quadrant area' A_q, and the x and y length scales for the sections are noted.

and is called the scaled Laplacian operator, with x_s and y_s being the conduit section length scales as identified in figure 3. The negative sign in (2.2) is included to ensure that negative pressure gradients produce positive average velocities $\langle w \rangle$. If Δ is scaled well, F_i is an $O(1)$ viscous resistance coefficient to be determined numerically for complex sections. However, for conduit sections of general convex shape, a sample of which are provided in figure 3, the Laplacian scaling approach of (2.2) is significantly more quantitative than other scaling methods such as the hydraulic diameter approach, and it can be shown that for many geometry types

$$F_i \equiv \frac{F_n}{3}\frac{A_q}{x_s y_s}, \tag{2.4}$$

where A_q is the quadrant section area (see shaded regions in figure 3), and $F_n \approx 1 \pm 0.1$ (Weislogel *et al.* 2008). An exact analytic or numeric value for F_n (or F_i) may always be employed if higher accuracy is demanded, but in many cases (2.4) is suitable for efficient design and analysis. In any case, the fact that F_n (or F_i) is nearly an $O(1)$ constant implies that a quantitative geometric dependence of $\langle w \rangle$ is captured by Δ_s in (2.2).

2.1. *Bulk rise: Lucas–Washburn*

For the pure bulk fluid capillary rise flow sketched in figure 1(*a*), ignoring capillary effects outside the tube, the pressure gradient term of (2.2) may be written as $P_z = -2\mathscr{H}\sigma/l$, where $2\mathscr{H}$ is twice the constant mean curvature of the free surface, σ is the surface tension, and $l = l(t)$ is the transient column length. Rewriting (2.2), the area-averaged velocity is

$$\langle w \rangle = F_i \frac{2\mathscr{H}\sigma}{l\mu\Delta_s}. \tag{2.5}$$

For a conduit of section area A_b, where subscript b denotes a bulk flow quantity, the well-known Lucas–Washburn diffusive power law solution is obtained by integrating (2.5), noting that $\langle w \rangle = \mathrm{d}l/\mathrm{d}t$ and $l(0) = 0$, to obtain the long-time transient advancing

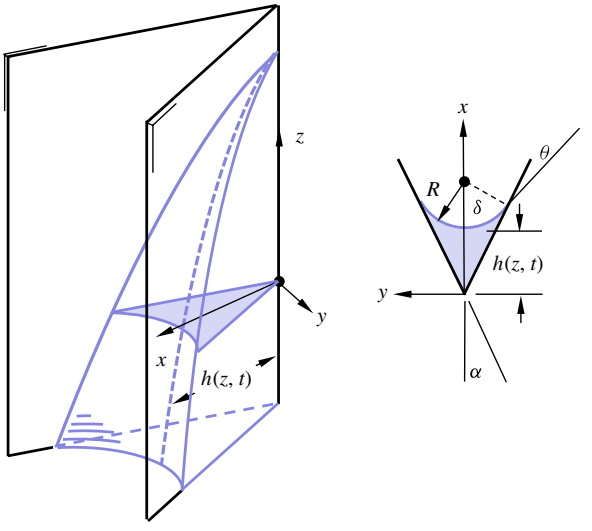

FIGURE 4. (Colour online) Sketch of capillary rise and cross-section in an interior corner with most of the pertinent notation. (Note that $x_s = h$, $y_s = h\tan\alpha$, and $R = fh$, where $f = \sin\alpha/(\cos\theta - \sin\alpha)$.)

bulk meniscus location and flow rate

$$l = \sqrt{2}\left(F_i\frac{2\mathscr{H}\sigma}{\mu\Delta_s}\right)_b^{1/2} t^{1/2}, \quad Q_l = \frac{A_b}{\sqrt{2}}\left(F_i\frac{2\mathscr{H}\sigma}{\mu\Delta_s}\right)_b^{1/2} t^{-1/2}. \tag{2.6}$$

For the special case of a circular cylindrical tube of radius r, $2\mathscr{H} = 2\cos\theta/r$, and for this representation, it may be shown that the exact analytic solution requires $F_i/\Delta_s = r^2/8$, i.e. Lucas–Washburn. Using (2.4) with $A_q = \pi r^2/4$, $x_s = y_s = r$, and $F_n \approx 1$, one estimates $F_i/\Delta_s \approx \pi r^2/24$. For calculating the bulk meniscus location $l(t)$ and flow rate Q_l, the error between the exact and Laplacian scaling solutions is 2 %. Again, exact viscous resistances may always be employed if greater precision is required, but the Laplacian scaling method does well to quickly capture the geometry-dependent viscous resistance of such flows, particularly as the geometric complexity increases.

2.2. *Corner rise*

For the pure interior corner capillary rise flow sketched in figure 1(*c*), slender columns of fluid rise along the interior corners, again enabling the quasi-steady flow approximation $w = w(x, y, t)$. An isolated corner flow cross-section is sketched in figure 4 for a corner of interior half-angle α, constant local radius of curvature $R = R(z, t)$, curvature angle $\delta \equiv \pi/2 - \alpha - \theta$, and meniscus centreline height $h = h(z, t)$. Again, (2.2) may be employed to quickly establish the form of the governing equation for such flow.

In this case, $P = 2\mathscr{H}\sigma = -\sigma/R = -\sigma/fh$, where the interface curvature function $f = \sin\alpha/(\cos\theta - \sin\alpha)$. Thus,

$$P_z = \frac{\sigma}{fh^2}h_z. \tag{2.7}$$

Choosing local scales $x_s = h$ and $y_s = h\tan\alpha$, it is found for the corner flow that

$$\Delta_s = \frac{1}{h^2} + \frac{1}{h^2\tan^2\alpha} = \frac{1}{h^2\sin^2\alpha}. \tag{2.8}$$

Substituting (2.7) and (2.8) into (2.2) yields

$$\langle w\rangle = -F_i\frac{\sigma\sin^2\alpha}{\mu f}h_z, \tag{2.9}$$

and from (2.4),

$$F_i \equiv \frac{F_n}{3}\frac{A_q}{x_s y_s} = \frac{F_n}{3}\frac{F_A h^2}{2h^2\tan\alpha} = \frac{F_n}{6}\frac{F_A}{\tan\alpha}, \tag{2.10}$$

where F_A is the corner flow geometric cross-section area function such that

$$A_c = F_A h^2, \quad F_A = f^2\left(\frac{\cos\theta\sin\delta}{\sin\alpha} - \delta\right), \tag{2.11}$$

where subscript c denotes a corner flow quantity. But $F_n \approx 1$ and $F_A/\tan\alpha \sim 1$ and from (2.10), $F_i \approx 1/6$. This value agrees favourably with the exact numerical solution of (2.1) for the corner flows, which yields $1/8 \lesssim F_i(\alpha,\theta) \leqslant 1/6$. Blindly applying a constant value $F_i \approx 1/7$ results in prediction errors of less than $\pm 7\,\%$ for all α and θ satisfying $\theta < \pi/2 - \alpha$. To repeat, the exact numerical value for F_i may always be applied if greater accuracy is desired, but the fact that F_i (or F_n) is such a weak function implies that the geometry of the cross-flow viscous resistance is correctly captured by length $\Delta_s^{-1/2} = h\sin\alpha$.

The local average velocity (2.9) may be substituted into a local volume balance equation $(A_c)_t = -(A_c\langle w\rangle)_z$, which after applying (2.11) yields the evolution equation for the corner flow meniscus height $h(z,t)$:

$$\left(h^2\right)_t = \frac{\sigma F_i\sin^2\alpha}{\mu f}\left(h^2 h_z\right)_z. \tag{2.12}$$

This form is applied in Weislogel & Lichter (1998), where the full details of the development may be found. The boundary conditions for (2.12) are the zero height condition at the advancing front where $h(z = \mathscr{L}, t) = 0$ and the constant height condition at the origin where $h(z = 0, t) = H$. The latter condition devolves from a constant pressure condition that is assumed at the origin and approximated using the explicit static zero-gravity equilibrium capillary curvature for such containers given by de Lazzer *et al.* (1996),

$$R(z_b, t) = \left(\frac{1}{2\mathscr{H}}\right)\Bigg|_{z=z_b} = \frac{P_b\cos\theta}{2\Sigma}\left(1 - \left(1 - \frac{4\Sigma A_b}{P_b^2\cos^2\theta}\right)^{1/2}\right) \equiv fH, \tag{2.13}$$

where in this case P_b is the perimeter of the container section, A_b is the container's cross-sectional area, and $\Sigma = mF_A/f^2$ is the total R-based corner flow area function (i.e. $A_c = F_A R^2/f^2$). Σ in (2.13) is written here specifically for containers with m identically wetted interior corners; a variety of such containers is illustrated in figure 5(*a–g*). These containers are dubbed m-regular containers, but the analysis holds for irregular sections such as the section of figure 5(*h*) as addressed in Weislogel (2001). The limitations of the use of the equilibrium (2.13) are given by Finn & Neel

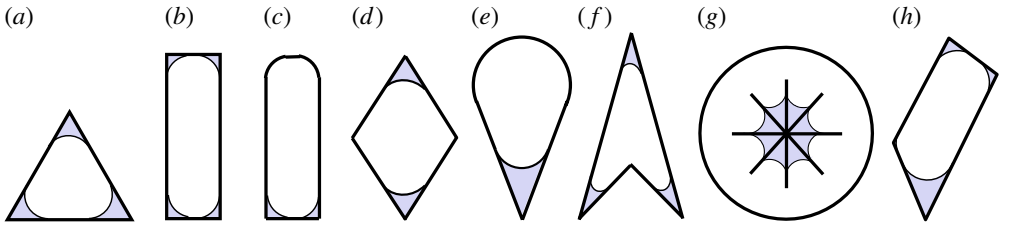

FIGURE 5. (Colour online) Selection of applicable container sections: (*a*) *n*-regular polygons, (*b*) rectangles, (*c*) combined rounded rectangles, (*d*) selective but equal-edge wetting sections, (*e*) $m = 1$ sections, (*f*) certain re-entrant sections, (*g*) vane structures, and (*h*) irregular polygonal sections. Sections (*a–g*) depict *m*-regular corner wetting geometries.

(1999), but its applicability as a boundary condition in dynamic flow problems is perhaps best demonstrated experimentally by Weislogel, Baker & Jenson (2011).

The numerical solution to (2.12) and boundary conditions determines the respective Lucas–Washburn-like transient length and flow rate of the corner flows:

$$\mathscr{L} = 1.702\left(F_i\frac{2\mathscr{H}\sigma}{\mu\Delta_s}\right)_c^{1/2} t^{1/2}, \quad Q_{\mathscr{L}} = 0.349mA_c\left(F_i\frac{2\mathscr{H}\sigma}{\mu\Delta_s}\right)_c^{1/2} t^{-1/2}, \tag{2.14}$$

where A_c, $2\mathscr{H}$ and Δ_s are evaluated at the origin where $z = z_b = 0$ and $h(0, t) = H$. Equation (2.14) agrees with experiments well within $\pm 6\,\%$ (see Weislogel & Lichter 1998 and Weislogel 2001).

Presented in this manner, (2.6) and (2.14) are clearly similar forms and suggest that the common $t^{1/2}$-dependence will also allow for solutions when such flows are combined. The corner flow results reviewed here apply under the primary global constraint of slender columns $(H/L)^2 \ll 1$, but further discussion is required to justify capillary pressure boundary conditions that might apply for the combined flow.

3. Model assumptions

In a recent work on quasi-steady capillary flows by Weislogel *et al.* (2011) it is re-demonstrated that for low capillary number flows ($Ca = \mu\langle w\rangle/\sigma \ll 1$) dynamic interface deflections are small and the bulk meniscus rapidly establishes a constant curvature that agrees well with that predicted by de Lazzer *et al.* (1996): see (2.13). It is argued that this constant curvature leads to a bulk meniscus region of fixed length. As the flow domain lengthens over time, i.e. $L \sim t^a$ where $a > 0$, the fixed length bulk meniscus region compresses to a line. This scenario is sketched in figure 6 for compound capillary rise in a square tube. In figure 6(*a*) the bulk meniscus centreline is denoted by z_{cl}, the location where the constant height location applies for the corner flow is denoted by z_b, and the tip of the advancing corner flow by z_{tip}. The present model for the flow is suggested in figure 6(*b*), where for slender flows $z_{cl} \approx z_b \approx l(t)$ and $z_{tip} - l(t) \equiv \mathscr{L}(t)$. The model of figure 6(*b*) leads directly to solutions for the compound flow provided that a variety of assumptions are satisfied. For example, for the bulk meniscus scaled by characteristic radius r, the flow must be sufficiently slender $(r/l)^2 \ll 1$ to neglect inertia $Su\,(r^2/Hl)^2/f \ll 1$ (Suratman number $Su \equiv \rho\sigma H/\mu^2$, where ρ is the liquid density), the volume of gas V_b in the bulk meniscus curvature region must be small, $V_b/lA_b \ll 1$ and $V_b/\mathscr{L}A_b \ll 1$, and the method of de Lazzer *et al.* must be applied to compute

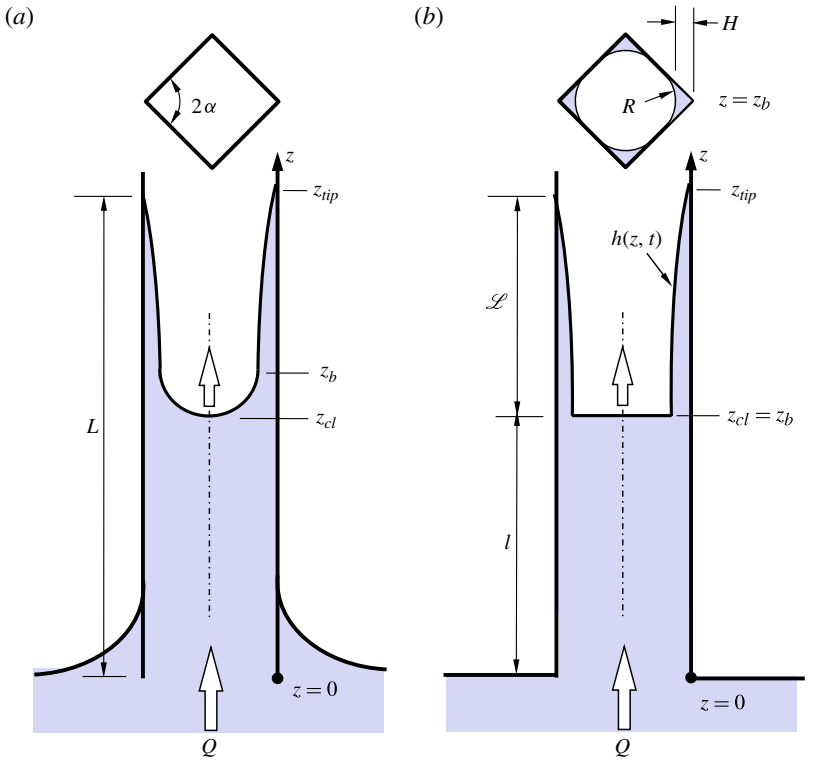

FIGURE 6. (Colour online) (*a*) Sketch of compound capillary rise in a square tube and (*b*) depiction of the model where the bulk interface region dimensions are neglected, but also where the static equilibrium capillary curvature and pressure conditions are applied.

the capillary curvature at the flat bulk meniscus $h(l(t)) = H$, (2.13). For the corner flow, the column too should be sufficiently slender, $(H/\mathscr{L})^2 \ll 1$, and possess low inertia, $Su\,(H/\mathscr{L})^2 \sin^4\alpha/f \ll 1$, and low streamwise free surface curvature, $(H/\mathscr{L})^2 f \ll 1$. Viscous normal stresses must be negligible for the bulk meniscus flow, $Ca_b \sim (r^2/Hl)/f \ll 1$, and the corner flows, $Ca_c \sim (H/\mathscr{L})^2 \sin^2\alpha \ll 1$. As a result, the static contact angle boundary condition θ may be applied everywhere. Gravity effects in all directions are neglected at present: $Bo_{zl} \equiv f\Delta\rho g_z Hl/\sigma \ll 1$, $Bo_{z\mathscr{L}} \equiv f\Delta\rho g_z H\mathscr{L}/\sigma \ll 1$, and $Bo_{xy} \equiv f\Delta\rho g_{xy} H^2/\sigma \ll 1$, where Bo is the Bond number, g_i denotes gravity in the i-direction or plane, and $\Delta\rho$ is the density difference between the displacing and displaced fluids. It is understood that if there is any finite negative acceleration component along the z-axis of the tube the bulk meniscus will ultimately achieve a fixed height where $Bo_{zl} \approx 1$. However, the corner flow(s) will continue to advance because of the ever-increasing capillary driving force as the corner is approached. In fact, the corner flow capillary pressure at the leading tip will balance the hydrostatic head such that $\sigma/fH_{\mathscr{L}} \sim \rho g_z \mathscr{L}$, which establishes an $\mathscr{L}$-dependent corner flow scale, $H_{\mathscr{L}} \sim \sigma/f\rho g_z \mathscr{L}$. Substitution of this scale into the visco-capillary balance of (2.9) for the corner flow, where $\langle w\rangle \sim \mathscr{L}/t$ and $h_z \sim H_{\mathscr{L}}/\mathscr{L}$, yields

$$\mathscr{L} \sim \left(\frac{\sigma^2}{\mu\rho g_z}\frac{F_i \sin^2\alpha}{f^2}\,t\right)^{1/3} \sim \left(\frac{\sigma^2}{\mu\rho g_z}(\cos\theta - \sin\alpha)^2\,t\right)^{1/3}, \tag{3.1}$$

as recently shown by Ponomarenko, Clanet & Quéré (2011), the right-hand term using (2.4). Therefore, $\mathscr{L} \sim t^{1/2}$ for the viscous advance when $Bo_{z\mathscr{L}} \ll 1$, but $\mathscr{L} \sim t^{1/3}$ when $Bo_{z\mathscr{L}} \gg 1$. The former is the focus of this work. All assumption criteria are readily assessed *a posteriori*, and most constraints are increasingly satisfied as the flows become increasingly slender with time.

4. Formulation

For a tube of cross-section A_b, in the Lucas–Washburn visco-capillary limit, a volume balance requires that the liquid volume flowing into the conduit is equal to the volume of the bulk flow plus the corner flows. For the model sketched in figure 6(*b*), this suggests that

$$\int_0^t Q \,\mathrm{d}\hat{t} = A_b l + m \int_l^{l+\mathscr{L}} A_c \,\mathrm{d}z, \tag{4.1}$$

where Q is the flow rate into the conduit, $l = l(t)$ is the length of the fluid column to the bulk meniscus, $\mathscr{L} = \mathscr{L}(t)$ is the length of the fluid column from the bulk meniscus to the advancing tip of the corner flow, and A_b and A_c are the total conduit and local corner flow section areas, respectively. The flow rate into the conduit is controlled by the bulk flow capillary pressure such that $Q = A_b \langle w \rangle$, with $\langle w \rangle$ determined from (2.5). Applying (2.11), (4.1) may be written as

$$A_b \left(F_i \frac{2\mathscr{H}\sigma}{\mu \Delta_s} \right)_b \int_0^t l^{-1} \,\mathrm{d}\hat{t} = A_b l + m F_A \int_l^{l+\mathscr{L}} h^2 \,\mathrm{d}z, \tag{4.2}$$

which is expressed and addressed in differential form in the Appendix. There is no length scale for the capillary rise problem in the zero-gravity limit. However, anticipating the $t^{1/2}$ power law, by choosing $L \sim l + \mathscr{L}$ and employing (2.6) and (2.14), the relation

$$L \sim \left[\left(F_i \frac{2\mathscr{H}\sigma}{\mu \Delta_s} \right)_b^{1/2} + \left(F_i \frac{2\mathscr{H}\sigma}{\mu \Delta_s} \right)_c^{1/2} \right] t^{1/2} \equiv (C_b' + C_c') t^{1/2} \tag{4.3}$$

may be used to determine a suitable time scale t_s. Choosing scales

$$z \sim L, \quad l \sim L, \quad h \sim H, \quad t_s \sim L^2 / (C_b' + C_c')^2, \tag{4.4}$$

and introducing dimensionless variables

$$z^* = z/L, \quad l^* = l/L, \quad \mathscr{L}^* = \mathscr{L}/L, \quad h^* = h/H, \quad t^* = t/t_s, \tag{4.5}$$

(4.2) may be rewritten as

$$\frac{1}{(1+\phi)^2} \int_0^{t^*} l^{*-1} \,\mathrm{d}\hat{t}^* = l^* + \beta \int_{l^*}^{l^*+\mathscr{L}^*} h^{*2} \,\mathrm{d}z^*, \tag{4.6}$$

where

$$\phi \equiv C_c'/C_b', \quad \beta \equiv m F_A H^2 / A_b. \tag{4.7}$$

The parameter ϕ is a ratio of corner flow to bulk flow viscous resistances and the parameter β is the corner flow saturation at the bulk meniscus. The conditions $\phi \ll 1$ and $\phi \gg 1$ appear to signal pure bulk and pure corner flow limits, respectively.

From (4.3) and (4.7),

$$\phi \equiv \frac{C_c'}{C_b'} \equiv \left(\frac{2\mathscr{H}\sigma F_i}{\mu\Delta_s}\right)_c^{1/2} \left(\frac{\mu\Delta_s}{2\mathscr{H}\sigma F_i}\right)_b^{1/2}. \tag{4.8}$$

But both flows are coupled by the shared capillary pressure at the bulk meniscus. Thus, $\mathscr{H}_b = \mathscr{H}_c$ and (4.8) reduces to

$$\phi = \left[\left(\frac{F_i}{\Delta_s}\right)_c \left(\frac{\Delta_s}{F_i}\right)_b\right]^{1/2} = \left[\left(\frac{A_q}{x_s y_s \Delta_s}\right)_c \left(\frac{x_s y_s \Delta_s}{A_q}\right)_b\right]^{1/2}, \tag{4.9}$$

where (2.4) with $F_n = 1$ has been applied to (4.9) in the rightmost term.

Equation (4.9) conveys that ϕ is the ratio of viscous cross-section length scales for the corner flow to the bulk flow, and since $A_q \sim x_s y_s$, it may be shown that

$$\phi \sim \left(\frac{\Delta_{sb}}{\Delta_{sc}}\right)^{1/2} \sim \left(\frac{A_c}{A_b}\right)^{1/2} \sim \beta^{1/2}, \tag{4.10}$$

where $0 \leqslant \beta \leqslant 1$. For the time being ϕ and β will be treated as independent parameters. However, it is clear from (4.10) that they are not for these compound capillary rise flows. Instead, from (4.9) it is observed that the corner flow section viscous length scale (i.e. $x_{sc} = H$) will depend on the bulk flow section viscous length scale (i.e. $x_{sb} = y_{sb} = r$), where the latter is presumably larger than the former, ensuring $\phi \leqslant 1$ and suggesting that conditions where $\phi > 1$ are non-physical for capillary rise as modelled by (4.2). Example flows in m-regular polygons and highly acute rhombic cylinders are invoked in § 8 to explore this point. An alternative flow rate formulation is employed in § 6 to pursue flows where in effect $\phi > 1$.

In terms of the (4.5) quantities the dimensionless corner flow equation (2.12) becomes

$$(h^{*2})_{t^*} = \frac{\phi^2}{(1+\phi)^2} (h^{*2} h^*_{z^*})_{z^*}, \tag{4.11}$$

subject to $h^*(l^*) = 1$ and $h^*(l^* + \mathscr{L}^*) = 0$. For known values of ϕ and β, (4.6) and (4.11) may be solved simultaneously for $h^*(z^*, t^*)$, $l^*(t^*)$ and $\mathscr{L}^*(t^*)$.

5. Similarity solution: capillary rise

For the boundary conditions of the present model, namely $h^*(l^*) = 1$, (4.6) and (4.11) yield to similarity under the diffusive power law transformation

$$h^* = F(\eta), \quad \eta = z^* t^{*-1/2}, \quad l^* = C_b t^{*1/2}, \quad \mathscr{L}^* = C_c t^{*1/2}, \tag{5.1}$$

where F and η are dimensionless similarity variables and C_b and C_c are unknown dimensionless transport coefficients for the bulk and corner flows, respectively (refer to the Appendix for details concerning coefficients C_b and C_c). Upon back-substitution, and defining $F' = \mathrm{d}F/\mathrm{d}\eta$, the local corner flow equation (4.11) becomes

$$\frac{\phi^2}{(1+\phi)^2} \left(F^2 F'\right)' + \eta F F' = 0, \tag{5.2}$$

subject to boundary conditions

$$F(C_b) = 1, \quad F(C_b + C_c) = 0, \quad F'(C_b + C_c) = -\frac{(C_b + C_c)}{2} \frac{(1+\phi)^2}{\phi^2}. \tag{5.3}$$

The third boundary condition is the tip slope condition, which is derived from (5.2) employing $F(C_b+C_c)=0$. Under these transforms the volume balance of (4.6) reduces to

$$\frac{2}{C_b\,(1+\phi)^2} = C_b + \beta \int_{C_b}^{C_b+C_c} F^2\,\mathrm{d}\eta. \tag{5.4}$$

The similarity system of equations (5.2)–(5.4) is solved by any number of methods to compute $F(\eta)$ and coefficients C_b and C_c. However, a slope discontinuity arises at the advancing front where $F \to 0$ and may cause difficulties. As in Romero & Yost (1996) and Weislogel & Lichter (1998), the solution method adopted here exploits the invariant nature of the corner flow equation, whereby introducing

$$F = \lambda^2 F^+, \quad \eta = \lambda \eta^+, \tag{5.5}$$

and defining

$$\lambda = C_b + C_c, \tag{5.6}$$

the transformed similarity corner flow equation (5.2) may be solved using a single backwards integration method from the tip where $\eta^+_{\mathscr{L}}=1$ and $F^+(\eta^+_{\mathscr{L}}=1)=\epsilon \to 0$. Defining $F^{+\prime}=\mathrm{d}F^+/\mathrm{d}\eta^+$, the unchanged invariant version of (5.2) becomes

$$\frac{\phi^2}{(1+\phi)^2}\left(F^{+2}F^{+\prime}\right)' + \eta^+ F^+ F^{+\prime} = 0, \tag{5.7}$$

subject to boundary conditions

$$F^+(1)=\epsilon \to 0, \quad F^{+\prime}(1) = -\frac{1}{2}\frac{(1+\phi)^2}{\phi^2}. \tag{5.8}$$

The invariant version of the first boundary condition listed in (5.3) may be used to find

$$C_b + C_c = \frac{1}{\left[F^+(\eta_b^+)\right]^{1/2}}, \tag{5.9}$$

where $F^+ \geqslant 0$ is noted and η_b^+ is the value of η^+ at the advancing bulk meniscus. Employing (5.9), the invariant version of the volume balance equation (5.4) becomes

$$\frac{2}{(1+\phi)^2}\frac{\left[F^+(\eta_b^+)\right]^3}{\eta_b^+} = \eta_b^+\left[F^+(\eta_b^+)\right]^2 + \beta\int_{\eta_b^+}^{1} F^{+2}\,\mathrm{d}\eta^+. \tag{5.10}$$

The procedure of the present method of solution is to set $\epsilon \lesssim O(10^{-6})$ and select desired values for ϕ and β. Equation (5.7) is then solved for $F^+(\eta^+)$. We then guess η_b^+, after which $F^+(\eta_b^+)$ is evaluated and substituted into the volume balance equation (5.10). The value for η_b^+ is adjusted and (5.10) is re-solved until satisfied to a desired convergence criterion, typically $\sim O(\epsilon)$. Converged values for η_b^+ are used to compute

$$C_b = \frac{\eta_b^+}{\left[F^+(\eta_b^+)\right]^{1/2}}, \quad C_c = \frac{1-\eta_b^+}{\left[F^+(\eta_b^+)\right]^{1/2}}, \tag{5.11}$$

from which $\eta_b^+ = (1 + C_c/C_b)^{-1}$ and the dimensional results for l, $\mathscr{L}$, and total flow rate Q are determined:

$$l = C_b(C_b' + C_c')t^{1/2} = C_b(1+\phi)C_b' t^{1/2}, \tag{5.12}$$

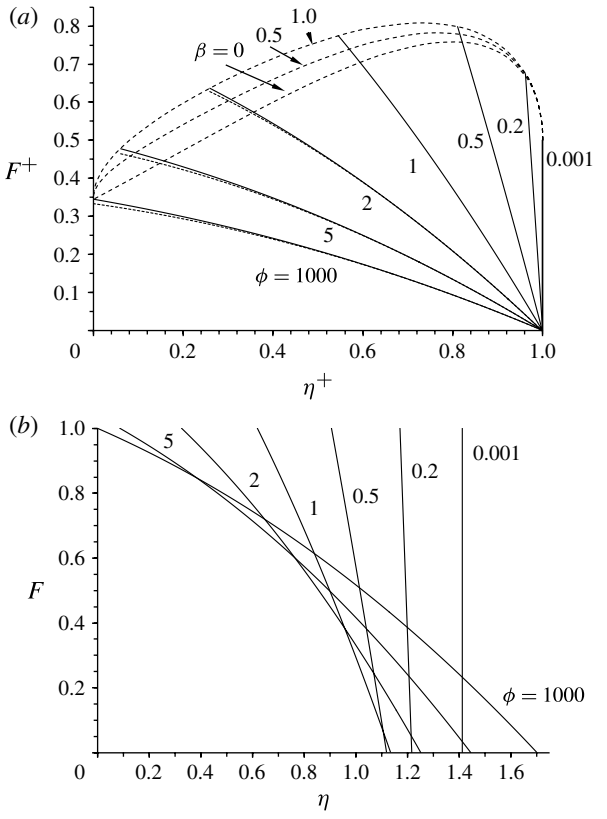

FIGURE 7. Numerical values for $F^+(\eta^+)$ and $F(\eta)$ as functions of ϕ and β. (*a*) The advancing corner flow profiles meet at $\eta^+ = 1$ for the selected values of ϕ indicated. The lower terminus of the corner flow region ($\eta^+ = \eta_b^+$) and the location of the advancing bulk meniscus are identified by the three dashed curves for selected values of β. The 4-term approximation of (7.2) is essentially coincident with all F^+ curves and the dotted lines shown in (*a*) display where the 2-term approximation is not coincident with the numerical results. (*b*) For $\beta = 1$, a pure (flat interface) bulk flow is observed for $\phi = 0.001$, where $\eta = \sqrt{2}$, and a pure corner flow is observed for $\phi = 1000$, where $F(\eta = 1.702) \approx 0$.

$$\mathscr{L} = C_c(C_b' + C_c')t^{1/2} = C_c(1+\phi)C_b' t^{1/2}, \tag{5.13}$$

$$Q = \frac{A_b C_b'}{C_b} t^{-1/2}. \tag{5.14}$$

Despite suspicions that $\beta^{1/2} \lesssim \phi \leqslant 1$ for compound capillary rise, numerical solutions for $F^+(\eta^+)$ and $F(\eta)$ for a selection of ϕ and β values are presented in figure 7 treating ϕ and β as independent parameters for $0 \leqslant \beta \leqslant 1$ and $0 \leqslant \phi \leqslant \infty$. Because (5.7) is independent of β, the $F^+(\eta^+;\phi)$ profiles in figure 7 are independent of β. But β does affect the range of the F^+ curves, as indicated by the three dashed lines drawn for specific values of $\beta = 0$, 0.5, and 1, where $F^+ = F^+(\eta^+;\eta_b^+,\beta)$. The increased linearity of the curves for F^+ and F for decreasing ϕ is evident in figure 7.

Numerical values for C_b, C_c, and $C_b + C_c$ are presented in figure 8 as functions of η_b^+. It is clear from figures 7(*b*) and 8 that $C_b + C_c \sim C_b \approx \sqrt{2}$ for $\phi \ll 1$ and $C_b + C_c \sim C_c \approx 1.702$ for $\phi \gg 1$. These are the expected asymptotic limits for pure

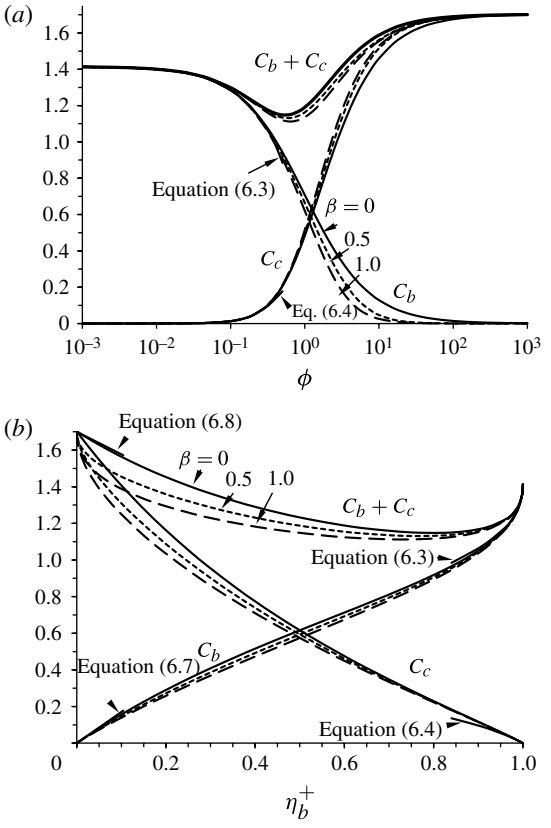

FIGURE 8. Numerical values for C_b, C_c, and $C_b + C_c$. (*a*) These coefficients are presented as a function of $0.001 \leqslant \phi \ll 1000$ for the three values of β noted. (*b*) The coefficients are presented as functions of η_b^+ also for the values of β noted. Where not coincident, the limiting asymptotic behaviour of (7.3)–(7.5) is provided as truncated curves for reference. Excellent agreement is achieved in the limits of large and small ϕ.

bulk flow equation (2.6) and pure corner flow equation (2.14), respectively. Following an alternative derivation for (5.10), these limits will be briefly explored before further discussion and application.

6. Alternative similarity solution: forced flow

An alternative approach to the above similarity solution assumes a diffusive power law form $Q = Q_o t^{-1/2}$ in (4.1) for what might be considered a forced or otherwise regulated flow at the tube inlet (refer to figures 1 and 6). With this choice, Q is independent of l. Choosing identical scales but replacing C_b' with $C_o' \equiv Q_o/A_b$, the volume balance of (4.6) may be rewritten as

$$\frac{2}{(1+\phi_o)} t^{*1/2} = l^* + \beta \int_{l^*}^{l^*+\mathscr{L}^*} h^{*2}\, \mathrm{d}z^*, \tag{6.1}$$

where $\phi_o \equiv C_c'/C_o'$. In invariant similarity form, (6.1) becomes

$$\frac{2}{(1+\phi_o)} \left[F^+(\eta_b^+)\right]^{5/2} = \eta_b^+ \left[F^+(\eta_b^+)\right]^2 + \beta \int_{\eta_b^+}^{1} F^{+2}\, \mathrm{d}\eta^+, \tag{6.2}$$

and compares with (5.10) for $\phi_o \lesssim O(1)$, where $\eta_b^+ > 0$. For cases where $\eta_b^+ \leqslant 0$, the forced inlet flow rate Q is less than or equal to the corner flow rate and the bulk meniscus recedes or remains stationary. For this situation the flow domain is dominated by the corner flow time scale, $C_b' = 0$, and for $\phi_o \gtrsim O(1)$, when $\eta_b^+ \leqslant 0$ one derives

$$\frac{2}{\phi_o} t^{*1/2} = l^* + \beta \int_{l^*}^{l^*+\mathscr{L}^*} h^{*2}\, \mathrm{d}z^*. \tag{6.3}$$

Equation (6.3) is solved along with (5.7) setting $\phi \to \infty$. For these receding flows $l \leqslant 0$, $\mathscr{L} \geqslant 0$, $C_c = 1/F^{+1/2}(0)$, and $C_b = \eta_b^+ C_c$.

In this way, from (6.2) and (6.3) similarity solutions are possible by control of Q_o via ϕ_o and are not restricted by the natural bulk meniscus capillary rise rate modelled by (4.1), which is singular at $l = 0$ (where $l^* = 0$, $C_b = 0$, and $\eta_b^+ = 0$). Equation (6.2) and (5.10) are equivalent when

$$\phi_o = \frac{(1+\phi)^2\, \eta_b^+}{[F^+(\eta_b^+)]^{1/2}} - 1. \tag{6.4}$$

The compound capillary rise solutions employing (5.10) are seen as a special case of more general solutions employing (6.2) and (6.3). The corner flow equation (5.7) subject to (5.8) remains unchanged with only ϕ_o replacing ϕ in the case of (6.2) and setting $\phi \to \infty$ in the case of (6.3). As in figure 7, numerical solutions to (5.7)–(5.8) and (6.2) for $\phi_o \geqslant 0$ are presented in figure 9 for $F^+(\eta^+)$ and $F(\eta)$, the difference being that the bulk meniscus can establish negative values in cases where the corner flow rates exceed those of the bulk meniscus.

7. Limit behavior of similarity solution

7.1. *Low corner flow limit,* $\phi^4 \ll 1$

When the corner flow is small compared to the bulk meniscus flow, ϕ is small, η_b^+ approaches 1, and it can be shown from (5.7) as it is observed from figure 7 that the advancing corner flow achieves a nearly linear profile. As demonstrated by Romero & Yost (1996), this profile may be approximated by an asymptotic analysis, and by rescaling (5.7) near $\eta_b^+ \to 1$, the naive expansion

$$F^+ = \frac{(1+\phi)^2}{\phi^2}[(1-\eta^+)F_0^+ + (1-\eta^+)^2 F_1^+ + (1-\eta^+)^3 F_2^+ + \cdots] \tag{7.1}$$

is used to solve (5.7) and boundary conditions (5.8) to find

$$F^+ = \frac{(1+\phi)^2}{\phi^2}\left[\frac{(1-\eta^+)}{2} - \frac{(1-\eta^+)^2}{6} + \frac{(1-\eta^+)^3}{108} + \frac{7\,(1-\eta^+)^4}{3240} + O\,(1-\eta^+)^5\right]. \tag{7.2}$$

Higher-order solutions may be obtained using the suggested form $F^+ = ((1+\phi)/\phi)^2 \sum_{i=1}^{\infty} K_i\,(1-\eta^+)^i$. This is fortunate because (7.2) for $F^+(\eta^+;\phi)$ is essentially coincident with the numerical results shown in figure 7 for all η^+ with maximum discrepancies of $\lesssim 0.1\,\%$. Retaining only the first two terms in (7.2), $F^+(\eta^+;\phi)$ is plotted in figure 7 using dotted lines. The curves are essentially

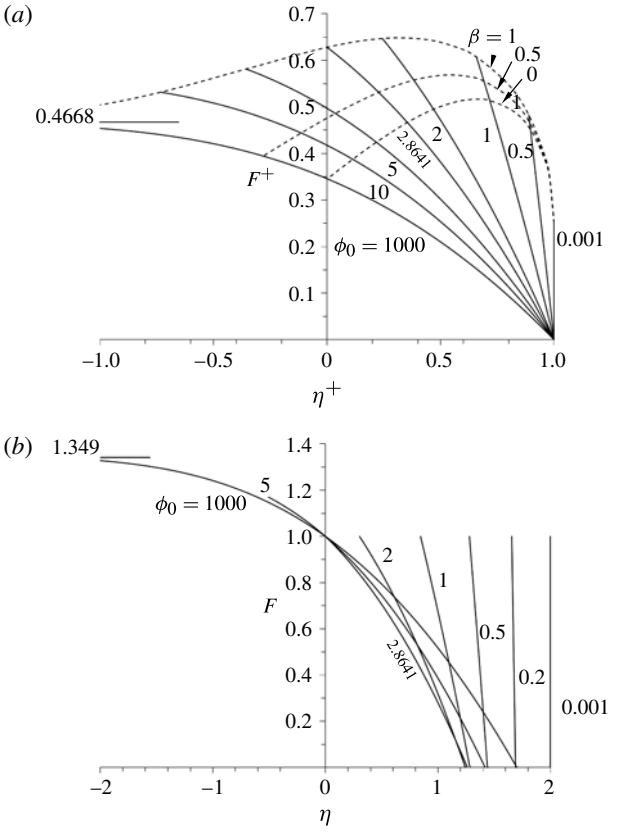

FIGURE 9. Numerical values for $F^+(\eta^+)$ and $F(\eta)$ as functions of ϕ_o and β for weakly forced flows. (*a*) The advancing corner flow profiles meet at $\eta^+ = 1$ for the selected values of ϕ_o indicated. The lower terminus of the corner flow region ($\eta^+ = \eta_b^+$) and the location of the advancing bulk meniscus are identified by the three dashed curves for selected values of β. Negative values for η_b^+ indicate a receding bulk meniscus and arise for $\phi_o \geqslant 2.8641$ when $\beta = 1$. $F(\eta)$ is presented in (*b*) where $F(C_b) = 1$ only when $C_b \geqslant 0$. When $C_b < 0$, only the condition $F(0) = 1$ is applied. $F(-\infty) \to 1.349$ as $\phi_o \to \infty$.

coincident for $\phi \lesssim 1$, with discrepancies increasing with further increases in ϕ, but remaining limited to $\lesssim 3\,\%$ even as $\phi \to \infty$ (despite the initial expectation of $\phi^4 \ll 1$). Thus the 2-term asymptotic expansion captures much of the parabolic nature of the corner flow profile and may be used to approximate F^+ for analytic solutions of η_b^+.

For example, substitution of the 2-term form of (7.2) for F^+ into the invariant volume balance equation (5.10) leads to a quartic equation for η_b^+. Only one root is positive and its cumbersome form is reduced significantly for small ϕ, producing

$$\eta_b^+ \approx 1 - \phi^2 + (5 - \beta)\frac{\phi^4}{3} + O(\phi^6), \tag{7.3}$$

which from (5.11) yields

$$C_b \approx \sqrt{2}(1 - \phi + \phi^2 - \phi^3) - \frac{\beta\phi^3}{3\sqrt{2}} + O(\phi^4), \tag{7.4}$$

$$C_c \approx \sqrt{2}(\phi^2 - \phi^3) + O(\phi^4). \tag{7.5}$$

The approximate equations (7.3)–(7.5) are represented by the nearly coincident truncated lines in figure 8 for $\phi \lesssim 0.4$. This 'low corner flow limit' yields β-independent solutions to $O(\phi^2)$, as is observed by the collapsing curves in figure 8(*a*) for small ϕ and in figure 8(*b*) as η_b^+ approaches 1. The results of (7.2)–(7.5) are accurate to $\lesssim 4\,\%$ for $\phi \lesssim 0.4$. This outcome is significant as will be discussed shortly. The generalized similarity solution of § 6 will not be pursued in this limit here.

7.2. *Low bulk flow limit, $\phi \gg 1$*

When the flow rate is dominated by the corner flows, ϕ is large, η_b^+ is small, and, in general, several limiting solutions are available. First, a useful zeroth-order solution is obtained in the small bulk flow limit where $Q \to 0$. This is the pure and complete corner rise flow addressed by Weislogel & Lichter (1998) and Weislogel (2001), but it is interpreted here as a compound capillary flow where the corner flows remove liquid from a receding bulk meniscus; see also Weislogel *et al.* (2011). From (5.10), provided that $\eta_b^{+2}\phi^2 \gg 1$, one observes

$$\eta_b^+ \left[F^+(\eta_b^+)\right]^2 + \beta \int_{\eta_b^+}^1 F^{+2}\,\mathrm{d}\eta^+ \approx 0. \tag{7.6}$$

When ϕ is large, F^+ takes a largely parabolic form and may be approximated by the 2-term parabolic (7.2) (see curve for $\phi = 1000$, figure 7). For improved accuracy, however, the zeroth-order fit for $\phi \to \infty$,

$$F^+ \approx 0.3463 - 0.2013\eta^+ - 0.1437\eta^{+2}, \tag{7.7}$$

may be used, which does well to satisfy all boundary conditions in (5.3) and is accurate for $-0.2 \leqslant \eta_b^+ \leqslant 1$ with errors $\lesssim \pm 1\,\%$. For solutions to (7.6), $\eta_b^+ \sim -\beta$, and often $\beta \ll 1$, and by applying F^+ of (7.7) to (7.6), it is found that

$$\eta_b^+ = -0.4097\beta - 0.2145\beta^2 + O(\beta^3). \tag{7.8}$$

This zero bulk flow condition was sketched in figure 1(*c*), where the bulk meniscus recedes with $t^{1/2}$.

A second useful solution in the low bulk flow limit may be obtained for a stationary bulk meniscus, where just enough fluid is pumped into the tube to balance the corner flow rate. In this situation $\eta_b^+ = 0$. But the left-hand side of (5.10) is singular in this limit unless it is observed that $\phi \sim [F^+(\eta_b^+)]^{1/2}/\eta_b^+$, which is not obvious unless the equivalent (6.1) is invoked to allow for Q values that are independent of l. In this case $\eta_b^+ = 0$, and (6.2) reduces to

$$\frac{2}{\phi_o}\left[F^+(0)\right]^{5/2} \approx \beta \int_0^1 F^{+2}\,\mathrm{d}\eta^+. \tag{7.9}$$

The solution to (5.7) with $\phi \to \phi_o \to \infty$ gives $\beta \int_0^1 F^{+2}\,\mathrm{d}\eta^+ = 0.04888\beta$ and $F^+(0) = 0.3451$, which when substituted into (7.9) yields the zeroth-order expression

$$\phi_o \approx \frac{2\left[F^+(0)\right]^{5/2}}{\beta \displaystyle\int_0^1 F^{+2}\,\mathrm{d}\eta^+} = \frac{2.8641}{\beta} = \frac{1}{0.349\beta}, \tag{7.10}$$

from which the stationary bulk meniscus flow rate may be determined from $Q_o = A_b C_o' = A_b C_c'/\phi_o$. Equation (7.10) recovers the exact solution of (2.14) for Q_o.

Lastly, for the capillary rise flow, substituting (7.7) into (5.10) and solving for $\eta_b^+ \ll 1$, it can be shown that

$$\eta_b^+ \approx \frac{1.671}{\beta\phi^2} + O\left(\beta\phi^2\right)^{-2}. \tag{7.11}$$

Expanding (5.11) for $\eta_b^+ \ll 1$ yields

$$C_b \approx 1.700\eta_b^+ + O(\eta_b^{+2}), \tag{7.12}$$

$$C_c \approx 1.700 - 1.228\eta_b^+ + O(\eta_b^{+2}), \tag{7.13}$$

where the parabolic curve fit error using F^+ from (7.7) produces a coefficient 1.700 compared to the numerical value 1.702. Thus, from (7.11) the low bulk flow limit solution is significantly more restrictive than the low corner flow limit solution requiring $\eta_b^+ \ll 1$, and arising when $1/\beta\phi^2 \ll 1$. For example, discrepancies of $\lesssim 3\,\%$ are maintained in (7.12)–(7.13) for $\phi \gtrsim 30$ ($\beta = 0.5$). Nevertheless, unless $\phi \to \infty$, the condition $\phi > 1$ may prove non-physical for compound capillary rise, as is addressed next for m-regular polygons and highly acute rhombic cylinders.

8. Discussion

The solutions presented in figures 7 and 8 are useful for quantitative assessment of the relative impacts of both bulk and corner flows for the compound capillary rise. The presence of the corner flow depletes the bulk flow in a way that appears to slow the advance of the bulk meniscus $l(t)$ as manifested through a reduced C_b value (see (5.12) and figure 8): $l \sim C_b$. However, the shorter column length of the bulk fluid reduces the bulk flow viscous resistance of the column, and the total flow rate into the conduit is increased by the combined flows as observed by inspection of the flow rate expression (5.14): $Q \sim C_b^{-1}$.

8.1. *n-regular polygons:* $n = 3, 4, 5 \ldots$

For n-regular polygonal conduits where each interior corner is wetted by the fluid, $m = n$ and $\alpha = \pi(m-2)/2m$. An advancing bulk flow arises when $\theta < \pi/2$ and m corner flows arise when $\theta < \pi/m$. When corner flows are present, $A_{qc} = F_A H^2/2$, $x_{sc} = H$ and $y_{sc} = H\tan\alpha$. For the bulk flow $A_{qb} = A_b/4$ and $x_{sb} = y_{sb}$. Recalling that $\beta = mF_{An}R^2/A_b$ and for regular polygons $A_b = P_b^2/4m\tan(\pi/m)$, substitution of these quantities into (4.9) reveals that

$$\phi = \left(\frac{2}{m}\beta\sin\left(\frac{2\pi}{m}\right)\right)^{1/2}. \tag{8.1}$$

Thus, ϕ depends on β which, from the definition of H from (2.13), may be computed for such sections as

$$\beta = \frac{\cos^2\theta}{F_{An}\cot(\pi/m)}\left[1 - \left(1 - \frac{F_{An}\cot(\pi/m)}{\cos^2\theta}\right)^{1/2}\right]^2, \tag{8.2}$$

where $F_{An} \equiv F_A/f^2$. For $\theta = 0$, values for β and ϕ are computed for selected values of m and listed in table 1, where it is observed that $\beta < \phi$ for all cases. For the square ($m = 4$), values are also computed and listed for selected values of the contact angle θ. Because $\phi^4 \ll 1$ and $\beta\phi^3 \ll 1$ are readily satisfied for such sections (see § 7.1), the advancing flows satisfy the conditions of the low corner flow limit, with (7.2)–(7.5)

m	θ	β	ϕ	ϕ^2	η_b^+	C_b	C_c	C_c/C_b
3	0	0.12514	0.26879	0.07225	0.93523	1.11299	0.07708	0.06925
4	0	0.06032	0.17366	0.03016	0.97126	1.20460	0.03565	0.02959
5	0	0.03630	0.11751	0.01381	0.98650	1.26541	0.01732	0.01369
6	0	0.02443	0.08397	0.00705	0.99303	1.30462	0.00916	0.00702
8	0	0.01333	0.04855	0.00235	0.99765	1.34872	0.00317	0.00235
10	0	0.00842	0.03146	0.00099	0.99901	1.37108	0.00136	0.00099
100	0	0.00008	0.00032	0.00000	1.00000	1.41383	0.00000	0.00000
4	0	0.06032	0.17366	0.03016	0.97126	1.20460	0.03565	0.02959
4	10	0.05381	0.16403	0.02690	0.97423	1.21465	0.03213	0.02645
4	20	0.03824	0.13827	0.01912	0.98146	1.24227	0.02346	0.01889
4	30	0.01911	0.09774	0.00955	0.99060	1.28826	0.01223	0.00949
4	40	0.00307	0.03916	0.00153	0.99847	1.36093	0.00208	0.00153
4	44	0.00015	0.00853	0.00007	0.99993	1.40225	0.00010	0.00007
4	44.5	0.00004	0.00431	0.00002	0.99998	1.40810	0.00003	0.00002

TABLE 1. Selection of values for $\phi = \phi(\beta; m, \theta)$ and accompanying computed results for η_b^+, C_b, and C_c from (5.7)–(5.11). All cases for n-regular polygons with m wetted interior corners ($n = m$). For all cases $\phi^4 \ll 1$, and predictions using (7.3)–(7.5) are accurate mostly to within 1 % (i.e. $\phi^2 \approx C_c/C_b$). θ is in degrees.

comparing well to the numerical solutions for η_b^+ and C_b with errors $\lesssim 1\,\%$, and for C_c with errors $\lesssim 3\,\%$. Thus, closed-form analytical solutions are available for such flows from (5.12)–(5.14), with ϕ and β determined from (8.1) and (8.2), and with C_b and C_c determined from (7.4) and (7.5). Useful closed-form results for $\phi^4 \ll 1$ may be expressed as

$$l \approx \sqrt{2}\left(\frac{2\mathscr{H}\sigma F_i}{\mu\Delta_s}\right)_b^{1/2} t^{1/2}, \tag{8.3}$$

$$\mathscr{L} \approx \sqrt{2}\,\phi^2\left(\frac{2\mathscr{H}\sigma F_i}{\mu\Delta_s}\right)_b^{1/2} t^{1/2}, \tag{8.4}$$

$$L = l + \mathscr{L} \approx \sqrt{2}(1+\phi^2)\left(\frac{2\mathscr{H}\sigma F_i}{\mu\Delta_s}\right)_b^{1/2} t^{1/2}, \tag{8.5}$$

$$Q \approx \frac{A_b}{\sqrt{2}}\left(\frac{2\mathscr{H}\sigma F_i}{\mu\Delta_s}\right)_b^{1/2} t^{-1/2}. \tag{8.6}$$

It is noteworthy that in this limit (8.3) and (8.6) are unchanged from their Lucas–Washburn pure bulk flow forms in (2.6), despite the presence of corner flows of observable extent. Despite their rapid advance, the corner flows represent a relatively low liquid volume which may be neglected with respect to the bulk flow in such situations. As observed from (8.3) and (8.4), the ratio of corner to bulk flow lengths is $\mathscr{L}/l \approx \phi^2$ in this limit. For comparison, ϕ^2 is listed with the exact numerical value of $\mathscr{L}/l = C_c/C_b$ in table 1. Disagreement is at worst $\lesssim 4\,\%$ for the equilateral triangle and diminishes quickly to zero for increasing m. The corner flows decrease in significance as m increases, and for all cases, as $\theta \to \pi/m$, $\eta_b^+ \to 1$, $C_b \to \sqrt{2}$, $C_c \to 0$, and the flow reverts to one of pure bulk capillary rise. Flow length ratios determined using $\mathscr{L}/l = C_c/C_b$ are quite small for n-regular sections, such as 0.0692 for the triangle and 0.0296 for the square, both for $\theta = 0$. It is not surprising that the

compound nature of such flows for, say, rectangular tubes goes unnoticed, since the corner flows extend only 3 % the distance of the bulk flow (Ichikawa, Hosokawa & Maeda 2004).

8.2. *Highly acute rhombi*

Thus, for m-regular polygon sections, ϕ may be computed to find that $\phi^4 = ((2/m)\beta \sin(2\pi/m))^2 \ll 1$, which yields nearly linear corner flow interface profiles. As was found for pure corner flows by Weislogel (2001), compared to regular polygonal sections, acute sections produce significantly higher corner flow imbibition rates. In fact, due to increases in β, over 20-fold increases in imbibition are predicted for highly acute rhombic sections when compared to square sections of the same cross-sectional area. To observe the nature of the compound flows for sections yielding higher values of both β and ϕ, such rhombic sections are briefly investigated here. Depending on the contact angle, corner flows in the highly obtuse corners are only present if the Concus–Finn condition $\theta < \alpha$ is also satisfied. Further, the volume of fluid in those corners is small, and is neglected for brevity in the present discussion. Otherwise, such flows would exhibit three different wetting conditions: $\theta < \pi/2$ for bulk flow, $\theta < \pi/2 - \alpha$ for acute corner flow, and $\theta < \alpha$ for obtuse corner flow.

A sketch of the corner flow rhombic section of side length a is provided in figures 3(*b*) and 5(*d*). ϕ for the flow is again defined by (4.9), where for the bulk flow $A_{qb} = (a^2/4)\sin 2\alpha$, $x_{sb} = a\sin\alpha$, and $y_{sb} = a\cos\alpha$. For these $m = 2$ acute corner flows $A_{qc} = F_A H^2/2$, where again $x_{sc} = H$ and $y_{sc} = H\tan\alpha$. Substitution of these quantities into (4.9) reveals that

$$\phi = \beta^{1/2} \tag{8.7}$$

and

$$\beta = \frac{\cos^2\theta}{F_{An}\sin(2\alpha)}\left[1 - \left(1 - \frac{F_{An}\sin(2\alpha)}{2\cos^2\theta}\right)^{1/2}\right]^2. \tag{8.8}$$

For $\theta = 0$, (5.7)–(5.11) are solved numerically for decreasing values of α and the results are listed in table 2. Despite the extremely acute limits where β approaches 1, ϕ remains $\lesssim O(1)$ and the corner flows never dominate to the extent that the flow would be considered in the 'low bulk flow limit' of § 7.2. From the Laplacian scaling perspective this is clear, since the corner flow section viscous length can never be larger than the bulk flow section viscous length. Thus $0 \leqslant \beta < \phi < 1$, and it is conjectured for capillary rise that the only time ϕ is greater than unity is when $\phi = \infty$ for the pure corner flow case. As $\theta \to \pi/2 - \alpha$, both β and ϕ decrease significantly, and the numerical coefficients approach their low corner flow limits, namely $\beta \to 0$, $\phi \to 0$, $\eta_b^+ \to 1$, $C_b \to \sqrt{2}$, and $C_c \to 0$. The θ-dependence is illustrated by the numerical values listed in table 2 for the $\alpha = 10^\circ$ rhombus.

9. Extension of method to hemiwicking in triangular grooves

Hemiwicking is a term employed by Quéré (2008) to categorize nearly all dynamic wetting across textured surfaces. Many such flows may be viewed as compound capillary flows and treated quantitatively by the present method. For a convenient example, capillary rise along grooved surfaces is a frequently studied problem, and a sample sketch of a triangular grooved surface is provided in figure 10 with groove depth d and width $2g$; see also Rye, Mann & Yost (1996) and more recently Liu *et al.*

α	θ	β	ϕ	ϕ^2	η_b^+	C_b	C_c	C_c/C_b
30	0	0.08771	0.29616	0.08771	0.92311	1.08973	0.09077	0.08329
20	0	0.16694	0.40858	0.16694	0.86748	0.99966	0.15272	0.15277
10	0	0.31702	0.56304	0.31702	0.78392	0.89140	0.24570	0.27563
5	0	0.46057	0.67865	0.46057	0.72022	0.81711	0.31742	0.38846
2	0	0.62066	0.78782	0.62066	0.66081	0.74984	0.38488	0.51329
1	0	0.71591	0.84612	0.71591	0.62917	0.71422	0.42095	0.58938
0.5	0	0.79039	0.88904	0.79039	0.60589	0.68798	0.44750	0.65046
0.1	0	0.90049	0.94894	0.90049	0.57337	0.65123	0.48456	0.74406
10	0	0.31702	0.56304	0.31702	0.78392	0.89140	0.24570	0.27563
10	10	0.31139	0.55802	0.31139	0.78668	0.89472	0.24261	0.27116
10	20	0.29590	0.54397	0.29590	0.79440	0.90407	0.23399	0.25881
10	30	0.27178	0.52133	0.27178	0.80682	0.91934	0.22013	0.23944
10	40	0.23910	0.48897	0.23910	0.82447	0.94159	0.20047	0.21291
10	50	0.19666	0.44346	0.19666	0.84901	0.97392	0.17320	0.17784
10	60	0.14172	0.37645	0.14172	0.88409	1.02420	0.13429	0.13111
10	70	0.07009	0.26475	0.07009	0.93704	1.11729	0.07507	0.06719
10	75	0.02880	0.16971	0.02880	0.97250	1.20886	0.03418	0.02828
10	79	0.00203	0.04508	0.00203	0.99797	1.35320	0.00275	0.00203
10	79.5	0.00056	0.02358	0.00056	0.99944	1.38164	0.00077	0.00056

TABLE 2. Values of $\phi = \phi(\beta; \alpha, \theta)$ and accompanying computed results for η_b^+, C_b, and C_c from (5.7)–(5.11). These cases are for highly acute rhombi where $\alpha \leqslant 30°$, that yield large values for ϕ. The results ignore corner flows in the obtuse corners of the rhombi. α and ϕ are listed in degrees.

(2011). When the surface is partially immersed in a wetting liquid, the fluid is drawn into and along the grooves in much the same manner as for the capillary rise in a tube: after sufficient time, the bulk meniscus establishes a constant curvature region of fixed length.

For the present analysis, the pivotal assumption requires that the fixed-length bulk meniscus region compresses to a line as time increases as illustrated in the model sketch in figure 10(*d*), as similarly modelled in figure 6(*b*). If this is the case, the bulk and corner flows are scaled by the same capillary pressure and the flow may be approximated by the present compound capillary flow method.

For these grooves the shared capillary pressure condition occurs where the interface just de-pins from the outer edge of the groove satisfying the contact angle condition, as depicted in the top views of figures 10(*b*) and 10(*d*). In this case, in like manner to the acute rhombic tubes, it may be shown again that $\phi = \beta^{1/2}$, since $R = g/\sin\delta$, and

$$\beta = F_{An} \tan\alpha / \sin^2\delta. \tag{9.1}$$

Despite large values for β for such flows, the fact that $\beta < 1$ ensures $\phi < 1$.

Romero & Yost (1996) analysed capillary flows in such open triangular grooves. Their analysis considers the pinned contact line up to the point where it detaches from the groove edge, becoming a free contact line corner flow from that point. A slope discontinuity at the junction between these regimes is a by-product of the solution, which is found to be Lucas–Washburn-like and yields to the $\sim t^{1/2}$ similarity transformation. From the compound capillary flow perspective the bulk flow instead maintains a constant cross-sectional area. Calculations for a variety of triangular grooves are performed using (5.7)–(5.10), and listed in table 3 for comparison

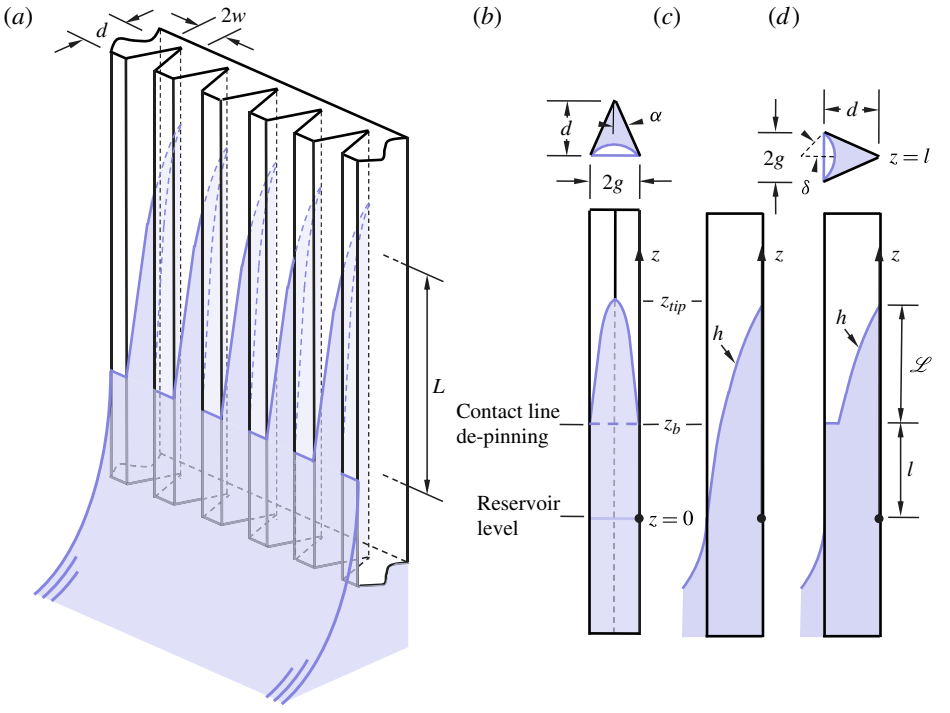

FIGURE 10. (Colour online) (*a*) Schematic of hemiwicking capillary rise along triangular grooves from the compound capillary flow perspective. (*b*) Free surface view of single groove flow with top view, (*c*) profile view, and (*d*) flow model profile view with top view and labels for bulk flow $l(t)$ and corner flow $\mathscr{L}(t)$.

with mostly limiting values determined from Romero and Yost (RY). In terms of the present analysis, η_{oRY} compares to $(C_b + C_c)(1 + \phi^{-1}) \equiv \eta_o^*$ and δ_{RY} compares to $(1 + C_c/C_b)^{-1} \equiv \eta_b^+$, where η_{oRY} is related to $l + \mathscr{L}$ and δ_{RY} is related to l. Discrepancies between the methods are typically $<2\,\%$, as seen by comparison of η_o^* with η_{oRY} and η_b^+ with δ_{RY} in table 3. It is clear from ratios C_c/C_b in table 3 compared to those listed in tables 1 and 2 that the corner flow comprises a larger proportion of the total compound flow length in open grooves compared to flows in closed conduits. For example, for $\alpha = 30°$, $\theta = 0°$, C_c/C_b values for an equilateral triangle, acute rhombus, and triangular groove are 0.0692, 0.0833, and 0.440, respectively. The highest values for C_c/C_b reported in table 3 are 0.833.

10. Compound capillary rise

From the specific calculations of the compound capillary rise in conduits of *n*-regular and acute rhombic section, and for the hemiwicking flows in triangular channels, it is clear that $\phi = \phi(\beta)$, where $\beta < 1$ and $0 \leqslant \beta < \phi < 1$, and thus the results of figures 7 and 8 for $\phi > 1$ are not currently imaginable for the combined flows. As a result, the form of solutions in (5.12) and (5.13) suggests that $C_b(1 + \phi)$ and $C_c(1 + \phi)$ are preferred coefficients which are re-plotted against ϕ in figure 11 for the stated conduits and open channels. The data reside along single curves representing the wide variations in container dimensions and contact angles.

α	θ	β	ϕ	η_b^+	C_b	C_c	η_o^*	η_{oRY}	δ_{RY}
15	0	0.69588	0.83420	0.63563	0.72149	0.41359	2.50	2.49	0.633
15	37.5	0.87598	0.93594	0.58044	0.65922	0.47651	2.35	2.34	0.579
15	75	1.00000	1.00000	0.54557	0.61970	0.51618	2.27	2.27	0.547
30	0	0.52721	0.72609	0.69440	0.78780	0.34660	2.70	2.68	0.689
30	30	0.79080	0.88927	0.60576	0.68783	0.44765	2.41	2.41	0.604
30	60	0.99999	1.00000	0.54557	0.61970	0.51618	2.27	2.27	0.547
45	0	0.42921	0.65514	0.73330	0.83210	0.30250	2.87	2.83	0.726
45	22.5	0.73269	0.85598	0.62382	0.70818	0.42706	2.46	2.46	0.622
45	45	0.99999	0.99999	0.54557	0.61970	0.51618	2.27	2.27	0.547
60	0	0.37240	0.61025	0.75798	0.86066	0.27480	3.00	2.95	0.749
60	15	0.69490	0.83361	0.63595	0.72185	0.41322	2.50	2.49	0.634
60	30	0.99998	0.99999	0.54557	0.61970	0.51618	2.27	2.27	0.547
75	0	0.34262	0.58534	0.77166	0.87677	0.25945	3.07	3.02	0.765
75	7.5	0.67355	0.82070	0.64295	0.72973	0.40524	2.52	2.51	0.642
75	15	0.99996	0.99998	0.54557	0.61970	0.51618	2.27	2.27	0.547
90	0	0.33467	0.57850	0.77542	0.88124	0.25523	3.10	3.04	0.764
90	0	0.66599	0.81608	0.64546	0.73255	0.40238	2.52	2.52	0.643
90	0	1.00000	1.00000	0.54557	0.61970	0.51618	2.27	2.27	0.547

TABLE 3. Computed values for hemiwicking in triangular grooves. Values from Romero & Yost (1996) denoted by *RY* are included for comparison. Note that α and θ are listed in degrees, and that agreement with the *RY* values is assessed by comparing η_{oRY} with $\eta_o^* \equiv (C_b + C_c)(1 + \phi^{-1})$ and δ_{RY} with η_b^+.

The $\phi^4 \ll 1$ asymptotic solutions of § 7.1 begin to fail by $\phi \gtrsim 0.4$, but a semi-analytic fit for the full domain $0 \leqslant \phi \leqslant 1$ is suggested by the third-order polynomial functions of (7.4) and (7.5), which when applied to the numerical data set of figure 11 yield curves that exactly satisfy the analytical solution as $\phi \to 0$ and are indistinguishable from the data with coefficients of determination equal to one. The fits show that

$$C_b = \frac{\sqrt{2}}{1+\phi}(1 - 0.0134\phi + 0.0904\phi^2 - 0.2003\phi^3), \tag{10.1}$$

$$C_c = \frac{\sqrt{2}\phi^2}{1+\phi}(1 - 0.2733\phi), \tag{10.2}$$

which implicitly account for β since $\phi = \phi(\beta)$. Such accurate fits arise from the single parameter ϕ, which is determined by a simple ratio of viscous cross-section length scales for the compound flow: see (4.9).

11. Summary

The corner flow solution of Weislogel & Lichter (1998) is combined with the classical Lucas–Washburn solution to describe capillary rise in tubes with interior corners. The solution is enabled by application of a constant curvature approximation in the overlap region between the bulk and corner flows. It is argued that this region is of fixed length which effectively shrinks to zero thickness as the flow lengthens with time. The model adds a volume balance equation to the corner flow equation, and through scaling identifies two parameters ϕ and β that may be determined *a priori* for a given system: ϕ is the ratio of viscous cross-section length scales between the corner and bulk flows and β is the corner flow saturation parameter at the bulk

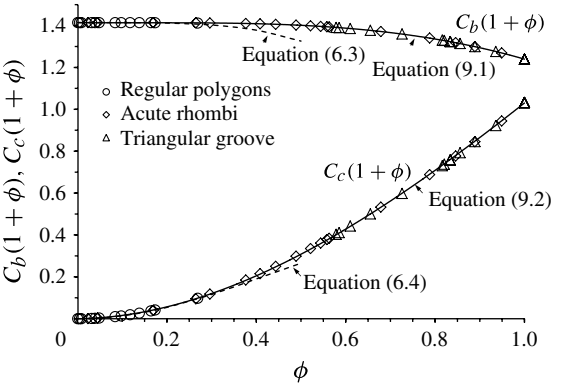

FIGURE 11. Coefficients $C_b(1+\phi)$ and $C_c(1+\phi)$ from (5.12) and (5.13) as a function of ϕ for compound capillary flow in conduits with n-regular polygonal and acute rhombic sections, and along grooved hemiwicking surfaces of triangular shape. All exact numerical solutions from tables 1–3 are shown (symbols) along with asymptotic solutions (truncated dashed lines). The semi-analytic fits agree with the data over the full range of ϕ with uncertainties typically <1 % (solid lines).

meniscus. It is found for typical conduit types that ϕ and β are not independent. A numerical similarity solution is solved, but for many practical flow conduits $\phi \lesssim 0.4$, and asymptotic expressions are available for the transient liquid column lengths and flow rates. As suggested by theory, an excellent third-order polynomial fit to the numerical data is accurate to $\pm \lesssim 1$ % for all practical values of $\phi \leqslant 1$, and produces

$$l = \sqrt{2}(1 - 0.0134\phi + 0.0904\phi^2 - 0.2003\phi^3)\left(\frac{2\mathscr{H}\sigma F_i}{\mu\Delta_s}\right)_b^{1/2} t^{1/2}, \tag{11.1}$$

$$\mathscr{L} = \sqrt{2}\phi^2(1 - 0.2733\phi)\left(\frac{2\mathscr{H}\sigma F_i}{\mu\Delta_s}\right)_b^{1/2} t^{1/2}, \tag{11.2}$$

$$Q = \frac{A_b}{\sqrt{2}(1 - 0.0134\phi + 0.0904\phi^2 - 0.2003\phi^3)}\left(\frac{2\mathscr{H}\sigma F_i}{\mu\Delta_s}\right)_b^{1/2} t^{-1/2}, \tag{11.3}$$

where $2\mathscr{H}$ is twice the mean curvature, F_i is an $O(1)$ numerical constant, and Δ_s is the scaled Laplacian operator for the bulk flow. Note that for the conduits of this investigation where $\phi < 1$, the influence of the corner flow on the overall flow rate equation (11.3) is weak, despite the corner flow length representing a significant proportion of the overall flow length equation (11.2).

The renowned Lucas–Washburn solutions for a single bulk meniscus are recovered for $\phi = 0$. The 'low corner flow' limit asymptotic solutions are recovered neglecting $O(\phi^3)$ terms, where $l(t)$ and $Q(t)$ are essentially unchanged from their Lucas–Washburn forms despite the $O(\phi^2)$ corner flows of negligible volume. In general, however, the exact Lucas–Washburn solution is recovered only when the bulk interface wetting condition $\theta \leqslant \pi/2$ is satisfied and no compound capillary flows are present, as is always the case for the right circular cylinder. For more complex conduit sections such as containers with interior corners of half-angle α, the Lucas–Washburn solutions are recovered only when the Concus–Finn corner wetting condition $\theta \leqslant \pi/2 - \alpha$ is not satisfied, whereupon $\beta = 0$ and thus $\phi = 0$. When $\theta \leqslant \pi/2 - \alpha$ is satisfied, capillarity-driven corner flows advance ahead of the bulk

meniscus, requiring the compound capillary flow approach. The approach outlined herein solves both advancing bulk and corner flows via application of a common capillary curvature (pressure) dynamical boundary condition. The corner flows remove liquid from the bulk with the appearance of slowing the fluid by reducing $l(t)$: see (11.1). However, the flow rate is actually increased due to the reduction of the bulk fluid viscous column length, as an increasing amount of the advancing fluid is distributed along the corners ahead of the bulk column during the process: see (11.3).

The present method serves as a model for both conduit and hemiwicking capillary rise flows. The ease with which the approach is applied to the latter argues favourably for its further development in this direction. In both cases, however, it is found that the viscous section length ratio ϕ depends on the corner saturation parameter β (i.e. $\phi \sim \beta^{1/2}$), and only in the case of pure corner flow imbibition does it seem that ϕ is ever greater than 1. In such instances, ϕ is infinite. An alternative similarity solution is offered in § 6 for weakly forced flows of the form $Q \sim t^{-1/2}$, where the dependence of ϕ on β is decoupled. But this direction is not pursued in depth here.

For capillary rise, for certain acute rhombic sections and triangular groove surfaces it is shown that $\phi = \beta^{1/2}$ with β determined by (8.8) and (9.1), respectively. The method succeeds by simplifying the geometric complexities of the bulk flow, and in particular the bulk curvature region which, for viscous flows, is essentially a finite length region which occupies a decreasing proportion of the flow that is lengthening with $t^{1/2}$. The viscous cross-section length ratio ϕ must be determined *a priori* and may be found by theoretical, numerical, or even experimental methods. Design-level accuracy is achieved quickly using the Laplacian scaling method employed herein.

Acknowledgements

This work was supported primarily by NASA under cooperative agreement NNX09AP66A managed by NASA's Glenn Research Center. Incremental contributions under previous funding sources such as NASA NNC05AA29A and NSF CTS-0521890 are also acknowledged. The alternative volume balance pursued in the Appendix was kindly brought to the author's attention by a referee. The author wishes to thank B. Weislogel for assistance with the computations and C. Poanessa and D. Wollman for drop tower experiment support. Conversations with colleague Y. Chen are appreciated. C. Poanessa and D. Wollman are supported by the NASA Oregon Space Grant Consortium grant NNX10AK68H.

Appendix

An alternative volume balance to (4.2) may be derived in terms of the corner flow rate. In this case a dimensional balance yields

$$mF_A \int_l^{l+\mathscr{L}} h^2 \,\mathrm{d}z = mF_A H^2 \int_0^t \langle w\rangle|_l \,\mathrm{d}\hat{t}, \tag{A 1}$$

where from (2.9)

$$\langle w\rangle|_l = -\left(\frac{F_i 2\mathscr{H}\sigma}{\mu\Delta_s}\right)_c \frac{1}{H}\frac{\partial h}{\partial z}\bigg|_l = -\frac{C_c'^2}{H}\frac{\partial h}{\partial z}\bigg|_l. \tag{A 2}$$

Substitution of (A 2) into (A 1) and non-dimensionalization yields

$$\int_{l}^{l^*+\mathscr{L}^*} h^{*2}\,\mathrm{d}z^* = -\frac{\phi^2}{(1+\phi)^2}\int_0^{t^*}\left.\frac{\partial h^*}{\partial z^*}\right|_{l^*}\mathrm{d}\hat{t}^*, \tag{A 3}$$

and (4.6) can be rewritten as

$$\frac{1}{(1+\phi)^2}\int_0^{t^*} l^{*-1}\,\mathrm{d}\hat{t}^* = l^* - \frac{\beta\phi^2}{(1+\phi)^2}\int_0^{t^*}\left.\frac{\partial h^*}{\partial z^*}\right|_{l^*}\mathrm{d}\hat{t}^*. \tag{A 4}$$

Differentiating (A 4) with respect to t^* and rearranging yields

$$(1+\phi)^2\, l^*\frac{\mathrm{d}l^*}{\mathrm{d}t^*} - \beta\phi^2 l^*\left.\frac{\partial h^*}{\partial z^*}\right|_{l^*} = 1. \tag{A 5}$$

The power law transform $\eta = z^* t^{*-1/2}$ of (5.1) converts (A 5) to

$$(1+\phi)^2\, t^{*1/2} l^*\frac{\mathrm{d}l^*}{\mathrm{d}t^*} - \beta\phi^2 l^* F'(C_b) = t^{*1/2}, \tag{A 6}$$

subject to $l^*(0) = 0$ and with $F'(C_b) =$ constant determined numerically from (5.2). A complementary solution to (A 6) yields

$$l^* = \frac{\beta\phi^2 F'(C_b)}{(1+\phi)^2}\left[3 - \left(1 + \frac{2\,(1+\phi)^2}{\left(\beta\phi^2 F'(C_b)\right)^2}\right)^{1/2}\right] t^{*1/2} \equiv C_b t^{*1/2}, \tag{A 7}$$

as expressed in (5.1), and converting to the $F^+(\eta^+)$ form

$$l^* = \frac{\beta\phi^2 F^{+\prime}(\eta_b^+)}{(1+\phi)^2 F^{+1/2}(\eta_b^+)}\left[3 - \left(1 + \frac{2\,(1+\phi)^2 F^+(\eta_b^+)}{\left(\beta\phi^2 F^{+\prime}(\eta_b^+)\right)^2}\right)^{1/2}\right] t^{*1/2} \equiv C_b t^{*1/2}. \tag{A 8}$$

Therefore,

$$C_b = \frac{\beta\phi^2 F^{+\prime}(\eta_b^+)}{(1+\phi)^2 F^{+1/2}(\eta_b^+)}\left[3 - \left(1 + \frac{2\,(1+\phi)^2 F^+(\eta_b^+)}{\left(\beta\phi^2 F^{+\prime}(\eta_b^+)\right)^2}\right)^{1/2}\right], \tag{A 9}$$

$$C_c = \frac{1}{F^{+1/2}(\eta_b^+)} - \frac{\beta\phi^2 F^{+\prime}(\eta_b^+)}{(1+\phi)^2 F^{+1/2}(\eta_b^+)}\left[3 - \left(1 + \frac{2\,(1+\phi)^2 F^+(\eta_b^+)}{\left(\beta\phi^2 F^{+\prime}(\eta_b^+)\right)^2}\right)^{1/2}\right]. \tag{A 10}$$

The simpler forms of (5.11) are preferred and pursued.

REFERENCES

Concus, P. & Finn, R. 1969 On the behaviour of a capillary free surface in a wedge. *Proc. Natl Acad. Sci.* **63**, 292–299.

Dong, M. & Chatzis, I. 1995 The imbibition and flow of a wetting liquid along the corners of a square capillary tube. *J. Colloid Interface Sci.* **172** (2), 278–288.

Finn, R. & Neel, R. W. 1999 C-singular solutions of the capillary problem. *J. Reine Angew. Math.* **512**, 1–25.

Ichikawa, N., Hosokawa, K. & Maeda, R. 2004 Interface motion of a capillary-driven flow in rectangular microchannel. *Colloid Interface Sci.* **280**, 155–164.

Kistler, S. F. 1993 *Hydrodynamics of Wetting*, *Surfactant Science Series*, vol. 49, pp. 311–430. Marcel Dekker.

DE LAZZER, A., LANGBEIN, D., DREYER, M. & RATH, H. J. 1996 Mean curvature of liquid surfaces in cylindrical containers of arbitrary cross-section. *Microgravity Sci. Technol.* **9** (3), 208–219.

LIU, W., LI, Y., CAI, Y. & SEKULIC, D. P. 2011 Capillary rise of liquids over a microstructured solid surface. *Langmuir* **27** (23), 14260–14266.

LUCAS, R. 1918 Ueber das Zeitgesetz des kapillaren Aufstiegs von Flüssigkeiten. *Kolloid Z.* **23**, 15–22.

PONOMARENKO, A., CLANET, C. & QUÉRÉ, D. 2011 Capillary rise in wedges. *J. Fluid Mech.* **666**, 146–154.

QUÉRÉ, D. 1997 Inertia capillarity. *Euro. Phys.* 533.

QUÉRÉ, D. 2008 Wetting and roughness. *Annu. Rev. Mater. Res.* **38**, 71–99.

ROMERO, L. A. & YOST, F. G. 1996 Flow in an open channel capillary. *J. Fluid Mech.* **322**, 109–129.

RYE, R. R., MANN, J. A. JR & YOST, F. G. 1996 The flow of liquids in surface grooves. *Langmuir* **12**, 555–565.

STANGE, M., DREYER, M. E. & RATH, H. J. 2003 Capillary driven flow in circular cylindrical tubes. *Phys. Fluids* **15**.

WASHBURN, E. W. 1921 The dynamics of capillary flow. *Phys. Rev.* **3** (2 XVII), 273–283.

WEISLOGEL, M. M. 2001 Capillary flow in containers of polygonal section. *AIAA J.* **39** (12), 2320–2326.

WEISLOGEL, M. M., BAKER, J. A. & JENSON, R. M. 2011 Quasi-steady capillarity driven flow. *J. Fluid Mech.* **685**, 271–305.

WEISLOGEL, M. M., CHEN, Y & BOLLEDULLA, D 2008 A better non-dimensionalization scheme for slender laminar flows: the Laplacian operator scaling method. *Phys. Fluids* **20** (2), 163–170.

WEISLOGEL, M. M. & LICHTER, S. 1998 Capillary flow in an interior corner. *J. Fluid Mech.* **373**, 349–378.

WOLLMAN, D. 2012 Capillarity-driven droplet ejection. Master's thesis, Portland State University.